

Christian Huber<sup>1</sup>, E M Parmentier<sup>1</sup>, and D Florez<sup>1</sup>

<sup>1</sup>Department of Earth, Environmental and Planetary Sciences, Brown University

January 26, 2024

## **Abstract**

Particle-fluid separation by settling is an ubiquitous process in Earth and Planetary Sciences. The rate of growth and the initial structure of cumulate layers in magma oceans or, over smaller scales, crustal magmatic systems depend on the crystal settling dynamics in melt-rich environments. The settling velocity of particles is controlled by a balance between buoyancy

1  
2 Particle sedimentation in a fluid at low Reynolds number: a generalization of  
3 hindered settling described by a two-phase continuum model.

4  
5 C. Huber, E.M. Parmentier, and D. Florez

6 Department of Earth, Environmental and Planetary Sciences, Brown University, RI, USA  
7

8 **Abstract**

9 Particle-fluid separation by settling is an ubiquitous process in Earth and Planetary Sciences. The  
10 rate of growth and the initial structure of cumulate layers in magma oceans or, over smaller  
11 scales, crustal magmatic systems depend on the crystal settling dynamics in melt-rich  
12 environments. The settling velocity of particles is controlled by a balance between buoyancy  
13 (contrast in density between phases) and drag forces. Since the seminal work of G. Stokes more  
14 than a century ago, parameterizations for the reduction of particle velocities caused by viscous  
15 dissipation due to their mutual interaction (hindrance) have commonly been described by a  
16 non-linear mapping between particle volume fraction and average particle settling velocity. In  
17 the present study we argue that these parameterizations neglect important physical behavior at  
18 high particle volume fractions, and as such are appropriate only when considering suspensions  
19 in which the particle volume fraction does not evolve dynamically in space or time. We  
20 introduce a more general model that accounts for the energy dissipation caused by changes in  
21 local particle volume fraction. This correction to hindered settling introduces a new term in the  
22 force balance (momentum conservation) that takes a similar form to compaction terms in two  
23 phase models at higher particle volume fraction and introduces a new consolidation or  
24 compaction viscosity that measures the resistance of the suspension to changes in solid volume  
25 fraction. Using idealized geometric models based on first principles, we derive closure equations  
26 for this effective compaction viscosity under both dilute and concentrated particle volume  
27 fraction limits. Through a series of numerical simulations, we show that the extended hindered  
28 settling model predicts two significant differences compared to traditional hindered settling  
29 models. First, while the steepening of particle volume fraction fronts observed with uncorrected  
30 settling remains, a dynamic instability (waves) is also generated at the front and travels at a  
31 slower velocity than the predicted hindered settling. This resolves the nonphysical,  
32 discontinuous behavior reflected by such fronts. Second, the rate of growth and structure of a  
33 cumulate layer growing above a no-flux (solid) boundary is strongly affected by the new  
34 compaction-like term of the model. In particular, the corrected model predicts the trapping of a  
35 higher volume fraction of interstitial melt in a correspondingly thicker cumulate layer.

36

37

38 **Key points**

- 39 1. A new model for particle settling proposed includes the effect of energy dissipation  
40 caused by solid volume fraction changes of the suspension in time and space that is not  
41 accounted for in traditional hindered settling.
- 42 2. The predicted settling velocities are significantly reduced compared to traditional  
43 models, especially when heterogeneous suspensions are considered.
- 44 3. The new model also introduces waves in particle volume fraction at oversteepening  
45 fronts that travel at a slower velocity than the discontinuous front predicted by hindered  
46 settling alone.

47

48 **1. Introduction**

49 The settling of particles in a fluid is a ubiquitous natural process. From sediments accumulating  
50 on a river or seabed (for low viscosity fluids) to the separation of crystals in melts in magma  
51 oceans or magma chambers, the processes governing the rate of fluid/solid separation by  
52 gravity have been studied for over 170 years.

53 The rate of particle settling and its dependence on the volume fraction of suspended particles  
54 exerts a fundamental control on the sedimentation rate and by extension on the porosity  
55 structure of the growing, sedimented layer. An analytical solution exists for the separation  
56 velocity of a single spherical particle in a boundless fluid otherwise at rest since the pioneering  
57 work of Gabriel Stokes in 1851 (section IV of “On the effect of internal friction of fluids on the  
58 motion of pendulums”). Particle settling, however, even at low particle volume fractions, is a  
59 difficult non-linear problem that does not admit analytical solutions. Therefore, most work  
60 focused on unraveling the rate of settling within a suspension (hindered settling) relies on  
61 empirical laws often inferred from experiments or tested experimentally under idealized  
62 conditions (e.g. Richardson and Zaki, 1954).

63 A common feature to all hindered settling models is the assumption of the existence of a unique  
64 mapping between the hindrance factor, which describes the reduction of the rate of settling for  
65 a given particle shape and size and for the volume fraction of suspended particles. The  
66 dependence of settling rate on particle volume fraction is generally cast in a power-law  
67 relationship. A variety of parameterizations have been provided from different studies (see  
68 review of Davis and Acrivos, 1985), some of these models include a critical volume fraction of  
69 particles beyond which settling is stopped (jamming conditions, e.g. Faroughi and Huber 2015)  
70 while others assume a finite separation velocity for any finite fluid fraction (e.g. Richardson and  
71 Zaki, 1954). These parameterizations have been used widely in many areas of the Earth and

72 planetary sciences for decades and therefore have had a large impact on our field as quickly  
73 summarized in the following paragraphs.

74 Particle settling plays a major role on sedimentation. Sedimentary deposits are commonly used  
75 as archives of past environmental conditions. Interrogating these archives through geochemical  
76 and textural analyses generally requires estimates of sedimentation rates as well as means to  
77 assess whether these archives are reliable and not overprinted by, for example, diagenetic  
78 processes. Sediments accumulated at the ocean bottom are often highly porous (small solid  
79 fraction) and it is not uncommon for the porosity to be significantly greater than 0.5 (Moore,  
80 1989; Dasgupta and Mukherjee, 2020). Ultimately, the porosity profile of the shallow sediments  
81 is controlled by (1) the deposition environment (composition and types of sediments) and the  
82 particle settling rate and (2) the reorganization of the porosity by consolidation shortly after  
83 deposition, both of which will be impacted by the corrected hindered settling model presented  
84 here.

85 In magmatic environments, settling is important to both bubble and crystal separation in the  
86 host melt (Marsh and Maxey, 1985; Martin and Nokes, 1989; Bergantz and Ni, 1999; Culha et al.,  
87 2020). Bubble-rich layers in laFor example, it is now well-accepted that crystal-melt separation  
88 is required to generate differentiated magmas (Bachmann and Bergantz, 2004; Hildreth and  
89 Wilson, 2007; Bachmann and Huber, 2016). The recent study of Lee and Morton (2015) argued  
90 based on the thermal longevity of intrusions and geochemistry that the crystal-melt separation  
91 that formed the high-silica granites in the Peninsular Range Batholiths (California) was largely  
92 influenced by hindered settling.

93 As in igneous intrusions, crystal sedimentation has been thought to play a major role in the  
94 evolution of early global scale magma oceans expected to form as planets accrete (Solomatov  
95 2000). This early evolution may have important consequences for long term planetary  
96 evolution. A progressively increasing Fe content, and thus increasing density of mafic mineral  
97 phases that crystallize from the residual liquid, would create unstable compositional  
98 stratification of mantle cumulates causing mantle overturn (Boukare et al. 2018; Elkins Tanton  
99 2012; Hess and Parmentier, 1995) and redistribution of trapped melt in cumulates.

100 Incompatible element concentrations due to melt that freezes into the cumulates control  
101 mantle trace element variability and radiogenic heat production which can influence planetary  
102 evolution on time scales much longer than that of magma ocean solidification. Moreover,  
103 settling and consolidation of liquid metal droplets in a magma ocean and possibly through  
104 partially molten silicate cumulates may form metallic cores (e.g. Rubie et al. 2003; Stevenson,  
105 1990). Buoyancy resulting from the competition between settling and convective mixing can  
106 control convective motions in solidifying core. Iron snow in planetary cores has been proposed  
107 as a mechanism to drive core convection and generate planetary magnetic dynamos. Huguet, et  
108 al. (2023) provide a recent summary of work relating to this process.

109 In this study, we revisit a major assumption underlying past treatments of hindered settling,  
110 specifically the existence of a unique relationship between particle volume fraction and settling

111 velocity. We argue that this assumption is valid only for suspensions that remain homogeneous  
112 (in terms of volume fraction) at all times. This is a serious limitation as these conditions are not  
113 satisfied for many applications of interest.

114 We develop a continuum framework based on two-phase theory to generalize the analysis of  
115 hindered settling to heterogeneous suspensions and most importantly the dynamic behavior of  
116 suspensions that develop heterogeneities in particle volume fraction over time. We find that  
117 while the standard models of hindered settling account for energy dissipation through the  
118 average drag between settling particles and the ambient viscous fluid, they do not account for  
119 the contribution of fluid drainage or accumulation when the volume fraction changes  
120 dynamically. We develop a general two-phase model that corrects hindered settling to account  
121 for the momentum dissipated by changes in local volume fraction. This model introduces a  
122 compaction-like consolidation viscosity (hereafter referred to as compaction viscosity), which  
123 depends on the fluid's viscosity and the local particle volume fraction. We derive three  
124 constitutive models to provide closure for the compaction viscosity and use the models to study  
125 the effect of this new, compaction-like, term on the settling rate of particles and the porosity  
126 structure of the resulting growing sediment layer form by the accumulation of particles. We  
127 compare our new model to the published, uncorrected, versions of hindered settling.

## 128 **2. Model Formulation**

### 129 2.1. Governing equations

130 Hindered settling is generally approached assuming that the ambient fluid is at rest or  
131 experiences a uniform velocity field (Richardson and Zaki, 1941; Batchelor, 1970; Guazzelli and  
132 Morris, 2012; Faroughi and Huber, 2015). Through a careful choice in reference frame (e.g.  
133 selecting that of the ambient fluid for example) and assuming an empirical description of the  
134 particles hindered velocity that depends only on the solid fraction  $X$

$$135 \quad V_H(X) = V_{st}H(X) \quad (1)$$

136 where  $V_H$  is the hindered velocity,  $V_{st}$  represents the Stokes velocity for a single particle and  
137  $H(X)$  is the hindrance function ( $0 \leq H(X) \leq 1$ ). Here, mass conservation is written as

$$138 \quad \frac{\partial X}{\partial t} + \frac{\partial [X v_H]}{\partial z} = \Omega. \quad (2)$$

139 In this expression  $\Omega$  is either null or includes effects such as subgrid scale dispersion of particles  
140 (below the scale of the representative elementary volume) or particle mass changes (growth,  
141 resorption).

142 We posit here that the modeling of hindered settling processes in a general way using equation  
143 (2) is flawed, built upon an assumption that does not fully account for the effects of  
144 heterogeneous particle distributions in space and time. This is because the empirical definition  
145 of  $V_H$  relies on the assumption that the particle volume fraction field is homogeneous in space  
146 (fixed and homogeneous  $X$ ). We show below that accounting for spatial and temporal

147 heterogeneities in particle volume fraction requires a two-phase approach and, specifically,  
 148 should include a correction on the stress acting on the particle field.

149 Starting from the framework of two-phase theory (Drew, 1983; McKenzie 1984; Bercovici, et al.  
 150 2001; Guazzelli and Morris, 2012; Wallis, 2020) we introduce 1-D mass conservation statements  
 151 (z along gravity) for the fluid

$$152 \quad \frac{\partial(1-X)}{\partial t} = - \frac{\partial((1-X)V_f)}{\partial z} \quad (3)$$

153 and solid

$$154 \quad \frac{\partial X}{\partial t} = - \frac{\partial[X V_s]}{\partial z} \quad (4)$$

155 assuming no mass exchange or source/sink in the system.  $V_f$  and  $V_s$  are the volume averaged  
 156 vertical (z) velocity component of the fluid (index f) or solid (s) fraction, respectively.

157 Neglecting inertia, the momentum conservation equations acting on each phase reads

$$158 \quad \frac{\partial((1-X)\sigma_{zz}^f)}{\partial z} + (1-X)\rho_f g - I = 0 \quad (5)$$

159 and

$$160 \quad \frac{\partial[X \sigma_{zz}^s]}{\partial z} + X \rho_s g + I = 0 \quad (6)$$

161 where  $\sigma_{zz}$  is the vertical normal stress acting on the phase,  $\rho_x$  is the density of a given phase and  
 162 I is the interphase force (normal + tangential force acting at interfaces). Here, the interphase  
 163 force is written as

$$164 \quad I = c(V_f - V_s) - P_f \frac{\partial(1-X)}{\partial z} \quad (7)$$

165 where c is a drag coefficient and  $P_f$  is the average fluid pressure. The difference of velocity  
 166 between the solid and fluid phase is generally considered as the hindered velocity

$$167 \quad V_H = V_s - V_f. \quad (8)$$

168 We define the normal vertical stress acting on the particles to be a perturbation to the fluid's  
 169 normal stress (where deviatoric stresses are neglected, i.e.  $\sigma_{zz}^f = -P_f$ )

$$170 \quad \sigma_{zz}^s = \sigma_{zz}^f + \Delta\sigma = -P_f + \Delta\sigma. \quad (9)$$

171 The perturbation  $\Delta\sigma$  represents the additional stress acting on particles associated with the  
 172 development of heterogeneities in the fluid/particle volume fractions. The development of such  
 173 heterogeneities requires work to be performed to increase or decrease the particle volume  
 174 fraction locally by draining interstitial fluid out of or into the control volume of interest. A  
 175 generic parameterization for  $\Delta\sigma$  is

176 
$$\Delta\sigma = \zeta \frac{\partial V_s}{\partial z}. \quad (10)$$

177 The scaling term in front of the divergence of the average particle velocity field has units of a  
 178 viscosity and mirrors the definition of a compaction stress and viscosity. While this  
 179 parameterization is similar to a compaction stress, it is easy to show that the material property  $\zeta$   
 180 is a function of the local particle volume fraction, permeability, fluid viscosity and particle size  
 181 (see next section). We will refer hereafter to  $\zeta$  as a compaction or consolidation viscosity.

182 After some algebra (supplements) we arrive at a two-phase description of the physics for  
 183 hindered settling

184 
$$\frac{\partial X}{\partial t} = -\frac{\partial[X V_s]}{\partial z}, \quad (11)$$

185 
$$\frac{\partial}{\partial z} [(1 - X)V_f + X V_s] = 0, \quad (12)$$

186 
$$\frac{c}{1-X} (V_f - V_s) + X \Delta\rho g + \frac{\partial}{\partial z} [X \zeta \frac{\partial V_s}{\partial z}] = 0. \quad (13)$$

187 The momentum conservation equation contains a characteristic length scale

188 
$$\delta = \sqrt{\frac{\zeta(1-X)^2}{c}} = \sqrt{\frac{\zeta}{\beta}} \quad (14)$$

189 where  $\beta = c/(1 - X)^2$ . The length scale  $\delta$  serves as a compaction length in this model. The  
 190 compaction length in a highly viscous compacting matrix with relatively small fluid fractions (e.g.  
 191 melt migration) is discussed by McKenzie (1984). The physical process here might be better  
 192 called consolidation rather than compaction, but we retain the use of compaction length since  
 193 this is a familiar term.

194 2.2. Closure model for the interphase drag: Hindered settling velocity

195 The closure of the two-phase continuum description for settling requires a model for the  
 196 interphase drag coefficient  $c$  in the governing equations (e.g. Eq. 13). Assuming that the solid  
 197 phase does not deform ( $\mu_s \rightarrow \infty$ ) the drag coefficient is expected to depend on the particle  
 198 shape and size ( $a$ ), the fluid viscosity,  $\mu_f$ , and the particle volume fraction,  $X$ .

199 We determine this coefficient using the limit where the particle volume fraction field  $X$  is  
 200 homogeneous ( $X \neq X(z)$ ) and the compaction term in the momentum conservation vanishes  
 201 (because  $\frac{\partial V_s}{\partial z} \rightarrow 0$ ). Under these idealized conditions, the momentum conservation can be  
 202 further simplified by recognizing that the average separation velocity between the two phases is  
 203 given by the uncorrected hindered settling velocity,  $V_H$ ,

204 
$$\frac{c}{1-X} (V_f - V_s) + X \Delta\rho g = -\frac{c}{1-X} V_H + X \Delta\rho g = 0 \quad (15)$$

205

206 where  $V_H=V_s-V_f$  is the uncorrected hindered settling velocity. This can be further expanded to

$$207 \quad \frac{c}{1-X} V_{Stokes} H(X) = X \Delta \rho g \quad (16)$$

208 where

$$209 \quad V_{Stokes} = \frac{2\Delta\rho g a^2}{9\mu_f} \quad (17)$$

210 for solid spherical particles. Therefore, the drag coefficient,  $c$ , can be determined from empirical  
211 hindered settling laws in homogeneous suspensions and yields

$$212 \quad c = \frac{9\mu_f X(1-X)}{2a^2 H(X)}. \quad (18)$$

213 The drag coefficient can alternatively be expressed as a “settling permeability”

$$214 \quad K_{settling} = \frac{2a^2 H(X)}{9X}. \quad (19)$$

215 A number of empirical expressions for the hindrance function,  $H(x)$ , relating normalized settling  
216 velocity and solid volume fraction have been published (see Davis and Acrivos, 1985). While  
217 most reproduce experimental data well at low solid fractions, their applicability to high solid  
218 volume fraction values is more ambiguous. For instance, while the parameterizations of  
219 Richardson and Zaki (1954) and Faroughi and Huber (2015) agree generally well at low volume  
220 fraction, the latter vanishes at a maximum packing fraction  $X_m$  while the former does not. We  
221 argue here that a proper parameterization for hindrance should retrieve familiar  
222 parameterizations of flow through a permeable, non-deformable medium at solid fraction near  
223 or in excess of the maximum packing. We construct a hindrance function parameterization that  
224 matches predictions from porous flow (Kozeny-Carman permeability parameterization) at high  
225 solid fraction and matches the hindrance parameterization of Faroughi and Huber (2015) at low  
226 to moderate particle fraction. This parameterization is given by Eq. (20a)

$$227 \quad H(X) = \frac{A(1-X)^2}{A+10X^2} \text{ with } A= 0.4 \text{ the relationship adopted here} \quad (20a)$$

228 and compared to the parameterization of Richardson and Zaki (1954)

$$229 \quad H(X) = (1 - X)^{4.65}, \quad \text{Richardson and Zaki (1954) for low } X \quad (20b)$$

230 and a hindrance function computed directly from the Kozeny-Carman permeability  
231 parameterization

$$232 \quad H(X) = \frac{(1-X)^2}{40X^2}, \quad \text{Kozeny- Carman permeability for } X \text{ approaching } X_m \quad (20c)$$

233 all plotted together in Fig. 1a.

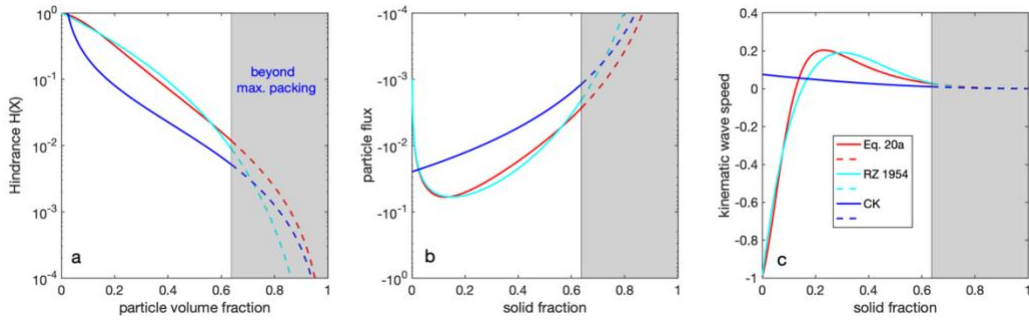
234 Written in terms of the hindered settling function, the mass conservation of solid reads

235 
$$\frac{\partial X}{\partial t} = -\frac{\partial}{\partial z} [V_s X] = -\frac{\partial}{\partial z} [V_{Stokes} H(X) X (1 - X)] = -\frac{\partial F_X}{\partial z} \quad (21)$$

236 where  $V_s = (1 - X)H(X)V_{Stokes}$  and  $F_X = V_{Stokes}H(X)X(1 - X)$ . Here,  $F_X$  is the particle flux  
 237 at depth,  $z$ . The particle flux as defined here is only a function of the particle solid fraction,  $X$ ,  
 238 and therefore

239 
$$\frac{\partial X}{\partial t} = -V \frac{\partial X}{\partial z} \quad (22)$$

240 which describes a kinematic wave for the solid volume fraction with speed  $V = \frac{\partial F_X}{\partial X}$ . Hindrance  
 241 functions, particle flux and kinematic wave speeds obtained using 20a are shown in Figure 1.



242  
 243 Figure 1. Illustration of the different closure models for the particle hindrance, particle flux and kinematic  
 244 wave speed. Panel a compares the settling model we propose in Eq. 20a to the Richardson and Zaki  
 245 (1954) empirical model (Eq. 20b) and a Kozeny–Carman model (Eq. 20c) for high particle volume  
 246 fraction. Panel b shows the particle flux as function of solid fraction for the same laws as in panel a.  
 247 Panel c shows the derivative of particle flux,  $F$ , with respect to solid fraction, which is defined as the  
 248 kinematic wave velocity for each of the same three models. The particle flux, and kinematic wave  
 249 velocity are negative because we take gravity to be directed along the negative  $z$ -direction.

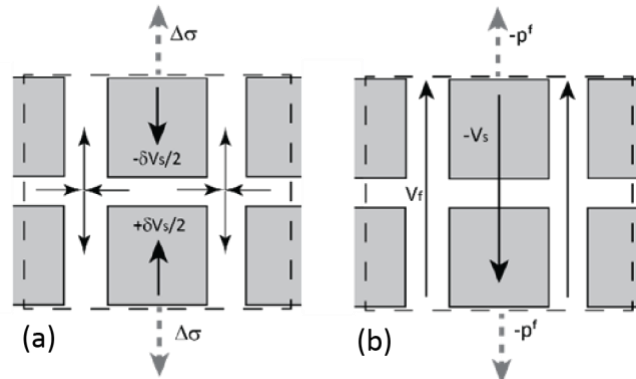
250

### 251 2.3. Closure models for the compaction viscosity with solid particles

252 The corrected version of hindered settling that we propose requires a definition for the  
 253 compaction viscosity  $\zeta$  to provide closure to the continuum conservation equations (11, 12, and  
 254 13). Intuitively, the compaction or consolidation viscosity must depend on the solid fraction (or  
 255 conversely the porosity), the size/mode of particles and on the fluid viscosity  $\mu_f$ . It shares the  
 256 same dimension and should be proportional to the fluid viscosity. Another important note here  
 257 is that the compaction viscosity,  $\zeta$ , should vanish at small particle volume fractions.

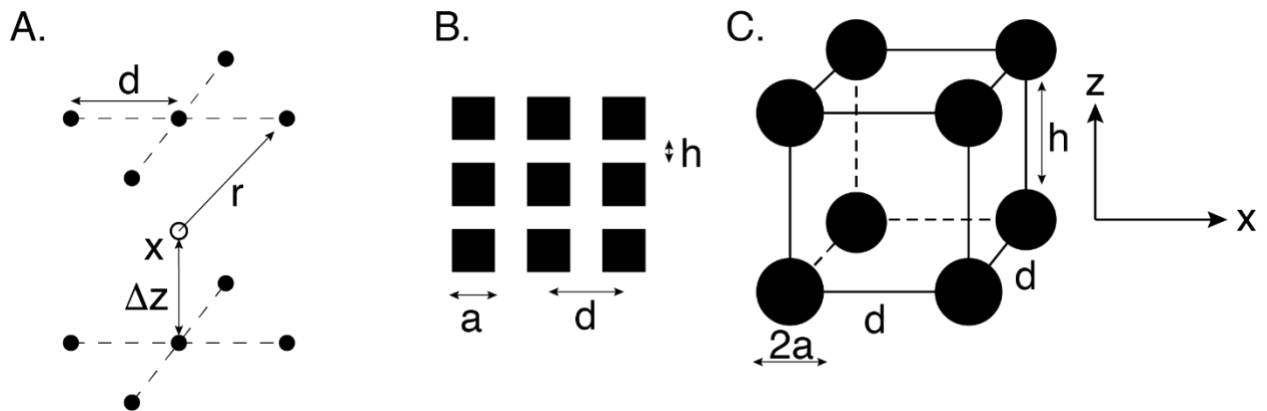
258 In this section, we discuss models to provide a closure to the compaction viscosity from first  
 259 principles using two general limits of solid fraction. The first model is based on the concept of  
 260 point forces in Stokes flow and provides a guide for the dependence of the compaction viscosity  
 261 on porosity in the limit of low particle volume fraction. The two other models provide  
 262 alternatives at high particle volume fraction, as the volume fraction approaches jamming  
 263 conditions.

264 Before discussing these closure models in detail, it is important to build a conceptual  
 265 understanding of how the forces that act on the particles are affected by changes in solid  
 266 fraction. As an illustration, we use the simple geometrical model shown in Figures 2. This highly  
 267 idealized geometry is particularly useful in distinguishing viscous dissipation associated with  
 268 consolidation/compaction from that for pure hindered settling. In panel X, blocks move with a  
 269 uniform vertical velocity corresponding to hindered settling alone. In panel X, particles that  
 270 settle with a vertically varying velocity. Hindered settling with compaction is described by the  
 271 superposition of the two.



272  
 273 Figure 2. Idealization illustrating the viscous flow imposed by compacting (or consolidating) and settling  
 274 in suspensions. On the right, all particles settle vertically with a uniform velocity  $V_s$  (REV shown by  
 275 the dashed lines) balanced by an opposing vertical flow between the particles  $V_f$ . The hindered  
 276 settling velocity  $V_s - V_f$  is determined by a balance between gravitational forces and the viscous  
 277 dissipation of vertical flow between the particles. This is contrasted with the scenario on the left  
 278 where the solid fraction decreases (particles get closer) because of a local perturbation in solid  
 279 velocity  $\delta V_s$ . Additional viscous dissipation is caused by fluid being expelled from closing spaces  
 280 between particles.

281 As shown in the following section, we find that the topology of the domain influences the  
 282 definition of the compaction viscosity but that there are some common characteristics that can  
 283 be used to develop a generic (idealized) closure model.



284

285 Figure 3. Geometrical models for the closure relationship between compaction viscosity and porosity. (A)  
 286 shows the 10 nearest neighbors model used for the limit of high porosity,  $x$  is the observation point.  
 287 (B) 2-D square model used for the limit of low porosity compaction viscosity and (C) with a simple  
 288 cubic lattice.

### 289 **Compaction viscosity at low solid fraction**

290 At low solid fraction, solid particles are far apart, i.e. if the particle size is  $a$  and the interparticle  
 291 (nearest neighbor distance) is  $d$ , then  $a/d \ll 1$  and the particle shape does not affect the flow in  
 292 the far-field. This limit allows for some useful simplifications. Most importantly it is possible to  
 293 consider that particles act as point forces on the fluid.

294 The pressure perturbation caused by a point force on the fluid at position  $x$  in a homogeneous  
 295 background flow with velocity  $V_p$  is (Batchelor, 1970; Guazzelli and Morris, 2012)

$$296 \quad \tilde{p} = \frac{3}{2} \mu_f a \frac{\vec{V}_p \cdot \vec{x}}{r^3} \quad (23)$$

297 where  $r$  is the distance between the particle (point force) and the observation point in the fluid,  
 298  $\vec{x}$ , and  $\mu_f$  is the fluid viscosity (see Figures 3 panel A). We now consider particles spaced far  
 299 apart on a simple cubic lattice and a smoothly spatially varying average separation velocity  
 300 between the fluid and the particles (non-homogeneous) such that

$$301 \quad V_{p,z}(z) \cong V_{p,z}(z_0) + \frac{\partial V_{p,z}}{\partial z} \Delta z, \quad (24)$$

302 where  $\Delta z = z - z_0$  and  $z_0$  is a point in the fluid centered between two layers of particles in the  
 303 lattice. The nearest 10 neighbors each contribute to the pressure perturbation to yield

$$304 \quad \tilde{p} = \frac{3}{2} \mu_f a \left[ \sum_{i=1}^5 -\frac{\partial V_{p,z}}{\partial z} \frac{\Delta z^2}{r_i^3} + \sum_{i=1}^5 -\frac{\partial V_{p,z}}{\partial z} \frac{(-\Delta z)^2}{r_i^3} \right]. \quad (25)$$

305 The two terms on the right-hand side are the contribution to pressure caused by the particle  
 306 above and below the reference position  $\vec{x}$ . With the configuration shown in Fig. 3a, the particle  
 307 volume fraction is expressed as

$$308 \quad X = \frac{4\pi a^3}{3\Delta z^3} \quad (26)$$

309 and, from equation 10, we get the compaction pressure (identifying the solid fraction velocity  $V_s$   
 310 to the continuum-scale particle velocity  $V_p$ )

$$311 \quad \Delta \sigma = \tilde{p} = \frac{3}{2} \mu_f \left( 2 + (\sqrt{2})^3 \right) \left( \frac{3}{4\pi} \right)^{1/3} X^{1/3} \frac{\partial V_s}{\partial z}. \quad (27)$$

312 This allows us to define, in this regime of low solid fraction, the compaction viscosity

$$313 \quad \zeta = \frac{3}{2} \mu_f \left( 2 + (\sqrt{2})^3 \right) \left( \frac{3}{4\pi} \right)^{1/3} X^{1/3} \quad (28)$$

314 which vanishes in the limit of  $X \rightarrow 0$  as expected. The geometric factors in the compaction  
 315 viscosity are a result of the arbitrary topology of the periodic arrangement of particles which  
 316 are roughly of order unity. Here,  $\zeta$  exhibits a linear dependence with respect to the fluid  
 317 viscosity (as expected in the Stokes flow regime) and a cubic root dependence with respect to  
 318 the particle volume fraction.

### 319 **Compaction viscosity at high solid fractions (approaching particle-particle contact)**

320 The first closure model that we explore for the limit of high solid fraction is based on a two-  
 321 dimensional periodic lattice of squares (see Figures 3, panel B). Assuming again that the  
 322 continuum approximation for the particle velocity is a smoothly varying function of the vertical  
 323 position  $z$  and given the definitions in Figures 3b,  $\Delta z = a + h$  is the vertical distance between  
 324 neighbor particle centers, and  $h$  is the gap between the particles. By definition, the change of  
 325 gap thickness over time is

$$326 \quad \frac{dh}{dt} = -\frac{\partial V_{p,z}}{\partial z} \Delta z = (a + h) \frac{\partial V_{p,z}}{\partial z}. \quad (29)$$

327 Using mass conservation of fluid in the gap

$$328 \quad \frac{a}{2} \frac{dh}{dt} = -\langle V_{f,x} \rangle h, \quad (30)$$

329 and defining the vertically averaged fluid velocity in the gap  $\langle V_{f,x} \rangle$

$$330 \quad \langle V_{f,x} \rangle = -\frac{h^2}{12\mu_f} \frac{\partial \Delta P_f}{\partial x}, \quad (31)$$

331 and the pressure drop can be approximated by

$$332 \quad \frac{\partial \Delta P_f}{\partial x} \cong \frac{\Delta P_f}{\frac{a}{2}}. \quad (32)$$

333 Again, identifying the continuum  $V_p$  with the solid fraction velocity  $V_s$  allows us to retrieve an  
 334 expression for the pressure perturbation caused by the heterogeneous solid fraction velocity  
 335 field

$$336 \quad \Delta \sigma = \Delta P_f = 3a^2 \frac{(a+h)}{h^3} \mu_f \frac{\partial V_s}{\partial z}. \quad (33)$$

337 Defining the particle volume fraction as

$$338 \quad X(h) = \frac{a^2}{(a+L)(a+h)}, \quad (34)$$

339 the compaction viscosity can be defined with respect to the particle volume fraction and a  
 340 maximum particle volume fraction ( $X_m = X(h \rightarrow 0) = 1 - \frac{L}{a+L}$ )

$$341 \quad \zeta = 3\mu_f X_m \frac{X^2}{(X_m - X)^3}. \quad (35)$$

342 As expected the compaction viscosity is proportional to the fluid depends linearly on the fluid's  
 343 viscosity but has a different dependence (stronger) on particle fraction and diverges as the  
 344 porosity approaches the residual porosity (no more vertical space to accommodate  
 345 compaction).

346 Simple cubic lattice of spherical particles

347 An alternative model can be derived for a simple cubic lattice of spherical particles. In this  
 348 model, with definition of the particle spacing illustrated in Figure 3c, the particle volume  
 349 fraction is

$$350 \quad X = \frac{4\pi a^3}{3d^2(a+h)}. \quad (36)$$

351 Assuming that the gap between particles  $h \ll a$  in the limit of porosity approaching the  
 352 jamming conditions (vertically), then we can use a lubrication approximation to use the same  
 353 argument as for the two-dimensional array of squares for the mass conservation

$$354 \quad \frac{a}{2} \frac{dh}{dt} = -\langle V_{f,x} \rangle h, \quad (37)$$

355 and using the average fluid velocity-pressure relationship obtained theoretically (and validated  
 356 numerically) by Zick and Homsy (1982)

$$357 \quad \frac{\Delta P_f}{a/2} = -\frac{9}{2} \frac{\mu_f}{a^2} c_{ZH} K \langle V_{f,x} \rangle, \quad (38)$$

358 with  $c_{ZH}$  a drag correction computed for a periodic array of spheres in Zick and Homsy (1982)  
 359 that is approximated by

$$360 \quad c_{ZH} \cong \frac{10 X}{(1-X)^3}. \quad (39)$$

361 With a maximum particle volume fraction

$$362 \quad X_m = \frac{4\pi a^2}{3d^2}, \quad (40)$$

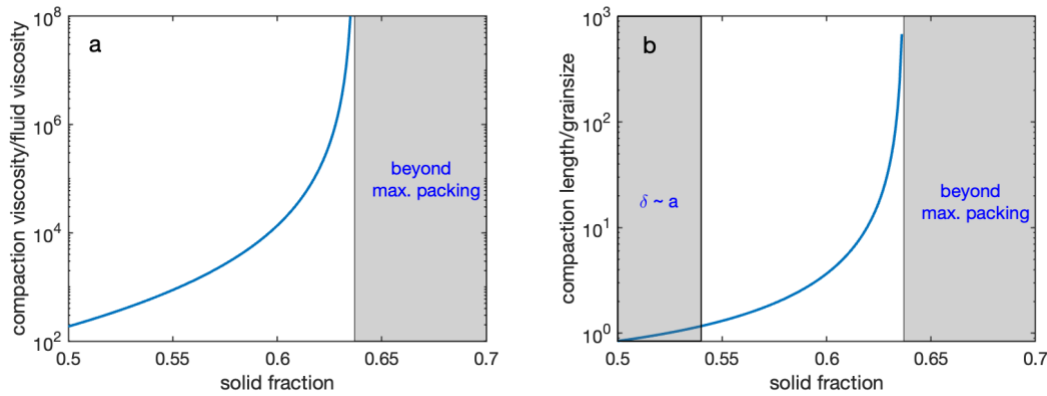
363 we get the compaction viscosity

$$364 \quad \zeta = \frac{45}{4} \mu_f \frac{X_m X^2}{(X_m - X)(1-X)^3}, \quad (41)$$

365 which diverges, as expected, when the particle volume fraction approaches  $X_m$ .

366 The compaction viscosity and the associated compaction length as function of the solid fraction  
 367 for the model with spherical particles (Eq. 41) is shown in Figure 4. One notes that the  
 368 compaction viscosity and therefore the compaction length are negligible at low solid fraction  
 369 and mostly matter near the maximum packing fraction.

370 It is interesting to note that the singularity as  $X \rightarrow X_m$  is much stronger in the simple cube  
 371 model,  $(X_m - X)^{-3}$  rather than  $(X_m - X)^{-1}$  for spherical particles. This suggests, not  
 372 surprisingly, that grain shape as well as grain size are likely to be important to the behaviors that  
 373 we describe below.



374  
 375 Figure 4. (a) Dependence of the compaction viscosity on the particle volume fraction, using the model in  
 376 equation (36). (b) Effective compaction length (normalized by particle size) as function of the  
 377 particle volume fraction for the same compaction viscosity as in the left panel.

378

### 379 3. Results

380 We conduct a series of numerical experiments to explore the behavior of settling with and  
 381 without compaction viscosity. Formulation of numerical methods applied to equations (11-13)  
 382 are summarized in Appendix 1; nondimensionalization of the equations is summarized in  
 383 Appendix 2. First, we consider a settling front in an infinite domain, and specifically the effect of  
 384 the compaction viscosity on the development of front instabilities and structure. Second, we  
 385 consider settling adjacent to a solid boundary and the effect of a compaction viscosity on the  
 386 formation and growth of a cumulate layer above that boundary.

#### 387 3.1 Stability and structure of a sedimentation front

388 To examine the role of compaction viscosity on the structure of a sedimentation front, we  
 389 consider the evolution of an initial depth distribution having the form of an error function with  
 390 solid fraction increasing both upward and downward. A layer with crystal fraction increasing  
 391 upward might form, for example, at the top of a mushy igneous intrusion where cooling of the  
 392 crystal-melt suspension at the top results in an upward increase in crystallinity. At large scales  
 393 similar behavior may be present in magma oceans which solidify by cooling at the planetary  
 394 surface. Solid fraction increasing downward could correspond with regions near the bottom of a  
 395 convecting magma ocean. Our objective here is not to consider either of these environments in  
 396 detail, but to examine suspension dynamics that could help better understand processes  
 397 occurring there.

399 These examples on an infinite domain assume a vanishing gradient in solid fraction at both the  
400 top and bottom implying that particles on the boundary settle at the hindered settling velocity.  
401 The reference frame in these infinite domains is defined by setting the fluid velocity to vanish at  
402 the lower boundary and therefore in the whole halfspace below the evolving front structure.  
403 Height along the vertical  $z$  coordinate is normalized by the reference compaction length. The  
404 settling direction is along the negative  $z$ -axis corresponding to a downward direction for gravity  
405 and velocity for particles that are denser than the fluid.

406 We first consider a simplified case where the compaction viscosity  $\zeta$  is constant ( $= \zeta_{ref}$ ). This  
407 is followed by a more general case where the compaction viscosity depends on the local particle  
408 volume fraction as inferred in section 2.2. As discussed above the compaction viscosity and  
409 corresponding compaction length are small for solid fractions well below the closest packed  
410 solid fraction  $X_m$ . At these low volume fractions the compaction length is expected to be  
411 comparable to the particle size (see Figure 4b). Under these conditions using a continuum  
412 approximation to describe the compaction behavior is inappropriate, thus we explore cases  
413 with high particle volume fraction near  $X_m$ .

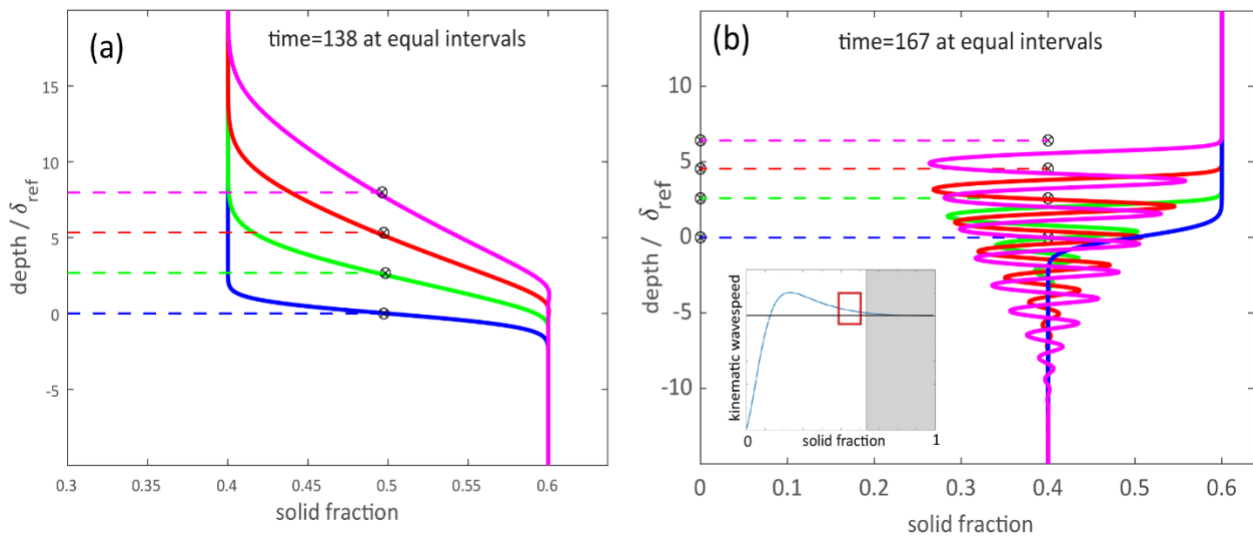
#### 414 **Constant compaction viscosity**

415 The evolution of a sedimentation front is controlled by both the compaction viscosity and the  
416 variation of the kinematic wave speed with solid volume fraction shown in Figure 1. Since the  
417 effects of compaction viscosity are most important at high solid volume fractions, we consider  
418 an initial solid fraction varying from 0.4 to 0.6 with a width of 2 reference compaction lengths.  
419 This range of solid fractions is above the kinematic wave speed maximum; the kinematic wave  
420 speed decreases with increasing solid volume fraction. Starting with the case shown in Figure 5a  
421 with solid fraction increasing in the settling direction (downward), particles in the low solid  
422 fraction region settle more rapidly than those in the higher solid fraction region beneath onto  
423 which settling particles accumulate. The front widens as it propagates upward into the region of  
424 lower solid fraction. If the initial front is approximated by small discontinuous steps in solid  
425 fraction, the lower magnitude of the wave speed at larger volume fractions (see inset in 5b and  
426 Figure 1 where a negative speed means a propagation direction opposite to settling) causes  
427 these parts of the front to be left behind so the front continuously broadens with time.  
428 Horizontal lines in Figure 5 mark the location of the finite amplitude kinematic wave front (see  
429 Figure 1 and discussion above) at each time shown.

430

431 With solid fraction decreasing in the settling direction, shown in Figure 5b, the opposite  
432 behavior occurs. Particles at depth settle more rapidly than those in higher solid fraction  
433 regions above. The higher kinematic wave speed magnitude at smaller particle volume  
434 fractions causes small steps of decreasing particle volume fraction to accumulate ahead of the  
435 steepening front. In the absence of a compaction viscosity, the front, as it propagates to

436 shallower depths, would steepen to a discontinuity that propagates at the kinematic wave  
 437 speed for a front of this amplitude. As in Figure 5a, horizontal lines mark the location of the  
 438 finite amplitude kinematic wave front at each time shown. With a nonzero compaction  
 439 viscosity, the initial front first steepens; but after reaching a width comparable to a few  
 440 compaction lengths, a system of trailing waves develops. This nearly harmonic-like wave train,  
 441 with a wavelength of several local compaction lengths, is initiated as the solid fraction at the  
 442 steepened front undershoots that behind the upward moving front. The wave behavior is a  
 443 consequence of the phase shift between compaction stresses and compaction rate implied in  
 444 the above discussion (equation 13). The front with nonzero compaction viscosity propagates at  
 445 a slightly slower speed than a purely kinematic discontinuous front of the same amplitude  
 446 reflecting the dissipation rate in the trailing wave train. Viscous dissipation also causes the wave  
 447 train to decay with distance behind the upward moving front.

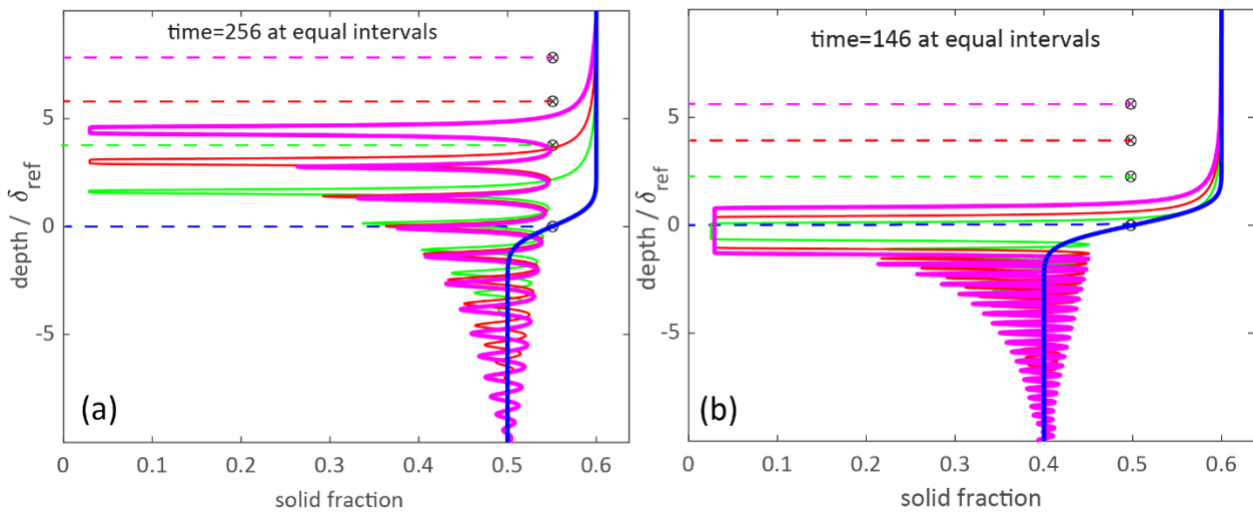


448  
 449 Figure 5. Evolution of an initial depth distribution of solid fraction with the form of an error  
 450 function varying between 0.4 and 0.6 with a width of 2 reference compaction lengths.  
 451 Colors blue through purple show the structure of the front at progressively longer times.  
 452 (a) initial solid fraction increasing in particle settling direction (downward). Dashed  
 453 horizontal lines at each time show the calculated location of a discontinuous front of this  
 454 amplitude propagating at its kinematic wave speed. (b) solid fraction decreasing in the  
 455 settling direction (downward).

456 This dispersive front behavior has also been described in numerical solutions for melt migration  
 457 (small fluid fractions in a continuous high viscosity matrix) by Spiegelman (1993). A more recent  
 458 detailed analysis of this behavior relevant to the rise of a buoyant fluid in a viscously deformable  
 459 conduit or melt migration is discussed by Lowman and Hoeffler (2013). The behavior that we see  
 460 here for particle consolidation at high solid fractions mimics the results reported in these earlier  
 461 studies. The analytical framework proposed in these previous studies should be helpful in a  
 462 more detailed study of the behavior described here and in the following section.

463 **Compaction viscosity varying with solid fraction**

464 As shown in Figure 6, a depleted (in terms of solid fraction) layer develops with a compaction  
465 viscosity that increases rapidly with increasing particle volume fraction, as  $X$  approaches  
466  $X_m$  (see Figure 4). The relatively uniform, depleted layer is bounded by two fronts as shown in  
467 Figure 6, but is most clearly developed in Figure 6b. These fronts include the initial front, as well  
468 as a second front that emerges with a particle density that increases in the settling direction.  
469 For the two cases shown the layer thickens more rapidly for the case with a greater contrast in  
470 solid fraction at the initial front. The lower layer progressively thickens while the solid fraction  
471 within the depleted layer remains nearly constant. The solid fraction within the depleted layer  
472 has nearly the same value for the two fronts of differing amplitude shown in panels a and b in  
473 Figure 6.



474

475 Figure 6. Evolution of an initial depth distribution of solid fraction with the form of an error function  
476 varying from 0.5 to 0.6 (panel a) and 0.4 to 0.6 (panel b) with the same width as in Figure 4 but with  
477 a compaction viscosity that increases strongly as solid fraction approaches the closest packed solid  
478 fraction (0.637 in this example). Compaction viscosity varies with solid fraction as shown in Figure 1  
479 and equation (42). As in Fig. 5 dashed horizontal lines show the calculated location of a  
480 discontinuous front propagating at the kinematic wave speed at each time. Note the  
481 reduced speed of the propagating front compared to the kinematic wave speed.

482

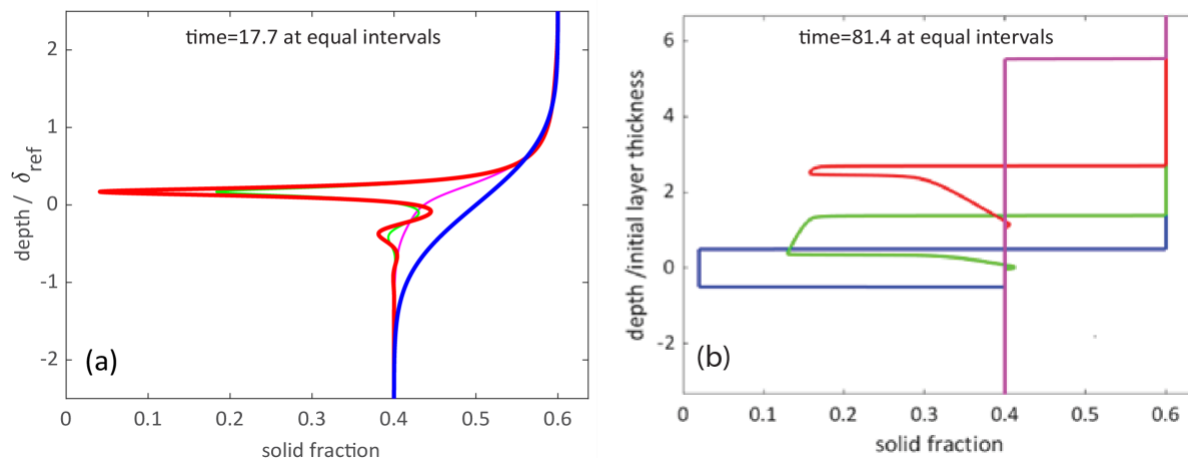
483 **Development of depleted layer**

484 The development of the depleted layer is intuitively reasonable since the particle flux for  
485 smaller solid fractions beneath the initial front is higher than at the larger solid fraction above it,  
486 creating the low solid fraction region between the fronts. However, understanding the structure  
487 of the two fronts and the development of a liquid-rich layer requires further study. The  
488 variation of kinematic wave speed with solid fraction (Figure 1) and the variation of compaction  
489 length and viscosity (Figure 4) may both play a role. Wave speed variation alone can result in

490 interesting behavior of kinematic front evolution (cf. Kynch 1952; Fitch 1983), but with a  
 491 constant compaction viscosity (Figure 5) the variation of wave speed alone does not show the  
 492 formation of a depleted layer. Furthermore, an initially prescribed, low solid fraction layer  
 493 defined by kinematic fronts (vanishing compaction viscosity) does not persist with time as shown  
 494 in Figure 7b. Thus, the variation of compaction viscosity with solid fraction appears to be an  
 495 essential component of this behavior.

496 As shown in Figure 7a, the early evolution of the initial front (blue) is reminiscent of that seen  
 497 above in Figure 5b, consisting of a damped wave train developing behind a steeping front. As  
 498 the trailing wave train amplitude increases with time the layer emerges as the solid fraction  
 499 decreases to values at which the compaction length is negligibly small. Note also that the  
 500 behavior of this trailing front is the opposite of that seen with constant compaction viscosity  
 501 (Figure 5) where the steepening of a front occurs only as the solid fraction increases in the  
 502 propagation direction.

503 Figure 7 (b) shows the behavior of a kinematic front initially containing a depleted (low solid  
 504 fraction) layer like that in Figure 6, but considering a case where the compaction viscosity is  
 505 vanishingly small and constant. Here, since the reference compaction length is negligible, the  
 506 vertical scale is normalized by the initial width of the layer. In the absence of a compaction  
 507 viscosity, both the thickness and amplitude of an initially prescribed low solid fraction layer  
 508 decays with time as the two kinematic fronts interact as shown here, again demonstrating the  
 509 fundamental role of compaction viscosity in the behavior seen in Figure 6.



510

511 Figure 7. (a) Early stages in development of the low solid fraction layer shown over longer times in  
 512 Figure 6b. The layer develops as growing waves (purple, green, then red) behind the initial front  
 513 (blue) reach a low solid fraction where the compaction length is small. The compaction viscosity  
 514 variation with solid fraction is that same as in Figure 6, with large values near  $X = X_m$  and small  
 515 vanishing small values for small  $X$ . As before horizontal lines denote the location of the kinematic  
 516 wave front at each corresponding time. Note that the dissipative waves along with the development  
 517 of the layer reduces the upward velocity of the settling front. (b) Evolution of initially prescribed low  
 518 solid fraction layer for vanishing compaction viscosity. Note that the initially imposed layer does not

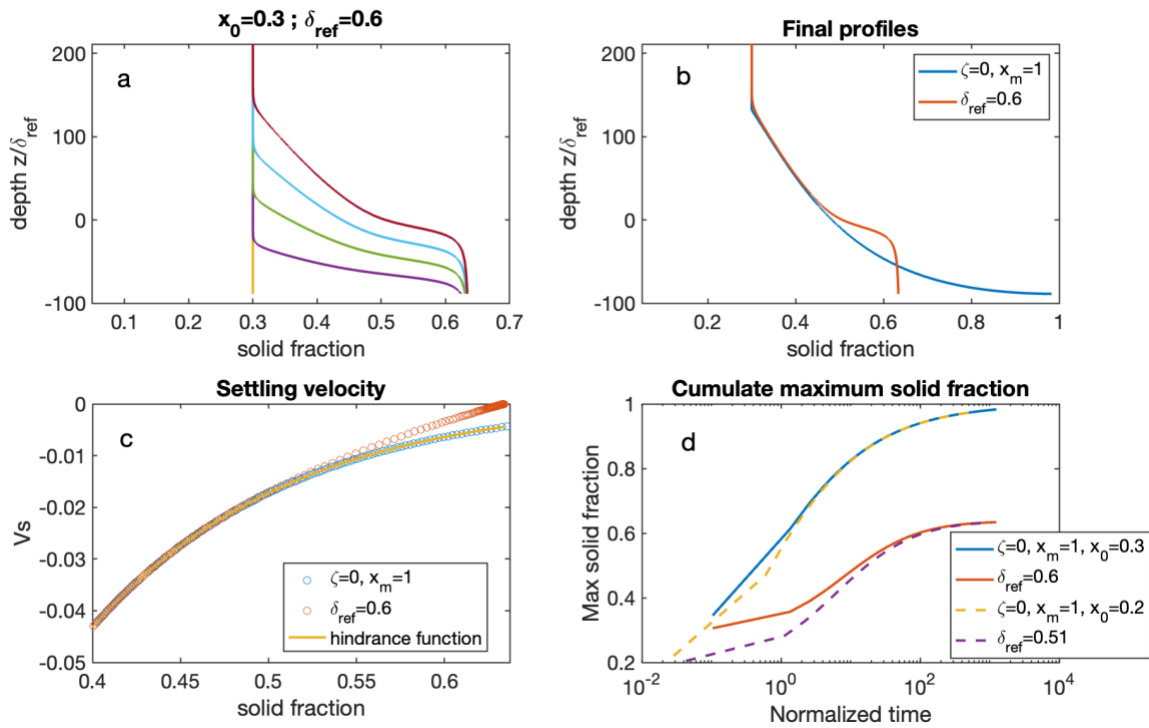
519        persist with time. The depth coordinate in this example with vanishing compaction length is  
520        normalized by the initial low solid fraction layer thickness.

521        One potentially important consequence of the development of a low solid fraction layer may be  
522        the buoyant Rayleigh-Taylor (RT) instability of such a low density, low viscosity layer (Whitehead  
523        1988; Wilcox and Whitehead, 1991; Lister and Kerr, 1989). The bulk viscosity in the depleted  
524        layer may be 4 to 6 orders of magnitude smaller (cf. Costa et al 2009, Faroughi and Huber, 2023)  
525        than in the higher particle fraction suspension above and below it. Since the wavelength of the  
526        fastest growing RT instability is proportional to the cube root of this viscosity ratio, the low  
527        viscosity of the layer can be expected to promote a long wavelength instability leading to phase  
528        segregation on a scale that should be several orders of magnitude greater than the layer  
529        thickness. Instability growth rate also increases with the layer thickness. Our numerical  
530        experiments suggest that the growth rate of the layer is nearly constant with time, whereas the  
531        growth rate of the RT instability will increase linearly with the layer thickness. Thus, when the  
532        layer thickness is large enough, the growth rate of RT instability should exceed the growth rate  
533        of the layer thickness so that we expect that RT instability can eventually control the dynamics  
534        of the layered suspension. The low viscosity in the layer should also promote incipient  
535        convective instability of the denser suspension above and below it.

### 536        **3.2 Growth of a cumulate layer by hindered settling**

537        The effect of the compaction viscosity correction on hindered settling is clearly visible in the  
538        structure of a growing cumulate layer above a solid (no flux) bottom boundary shown in Figure  
539        8. Both the layer thickness and trapped melt distribution are drastically different when the  
540        effect of compaction/consolidation is included. The effective settling velocity versus solid  
541        fraction departs from the hindrance function only at high solid fraction with the compaction  
542        correction, which is not surprising given the fact that the compaction viscosity and compaction  
543        length are significantly greater for these values (Figures 3), which amplifies the relative  
544        contribution of the compaction term in the momentum conservation equation. At high solid  
545        fraction the settling velocity vanishes at  $X_m$  because it marks the limit where compaction by  
546        settling is no longer possible as the suspension reached its maximum packing fraction. Without  
547        the compaction term, settling is controlled solely by the hindrance function which continuously  
548        and monotonously decreases to 0 when the solid fraction reaches 1. In the absence of a  
549        compaction term in the momentum conservation, the cumulate layer can reach a solid fraction  
550        of 1, well beyond the maximum packing of the solid particle suspension. This is unphysical  
551        because there is no prescribed compaction model to consider consolidation past the maximum  
552        packing here. In contrast, the consideration of the compaction term in the momentum  
553        conservation limits the maximum solid fraction to the prescribed maximum packing value, a  
554        suspension under settling alone cannot reach a solid fraction beyond the maximum packing.  
555        The curvature of the solid fraction depth profiles differs significantly when the solid fraction of  
556        exceeds about 0.5 in this example. The profile is concave without compaction, while it is convex  
557        and pinned to the maximum packing fraction otherwise. The degree of curvature depends on

558 the effective compaction length with depth over the lower section, a greater compaction length  
 559 leading to a lower maximum curvature while a smaller compaction length would generate a  
 560 more step-like transition from the cumulate layer to the settling suspension.



561  
 562 Figure 8. (a) Solid fraction that accumulates in a layer adjacent to a solid (no flux) boundary beneath a  
 563 halfspace in which the initial solid fraction has the uniform values 0.3, this case includes a solid  
 564 fraction dependent compaction viscosity. (b) Comparison of solid fraction distribution with (red) and  
 565 without (blue) the effect of compaction viscosity on hindered settling. The blue curve compares the  
 566 solid fraction without compaction viscosity with the final time in (a). (c) Deviation of local settling  
 567 velocity (red circles) from that predicted by the hindered settling function without compaction  
 568 viscosity (blue line). (d) Evolution of the maximum solid fraction in the cumulate over time for 4  
 569 simulations, the blue and red lines show the case with a starting homogeneous solid fraction of 0.3  
 570 and with and without compaction respectively and the orange and purple dashed lines show the  
 571 case a starting homogeneous solid fraction of 0.2 with and without compaction.

572 The lower right panel of Figure 8 shows the maximum solid fraction in the profile as function of  
 573 time considering four different cases. Here runs with an initial solid fraction of 0.2 and 0.3 are  
 574 compared to equivalent runs where the compaction viscosity was set to 0 (uncorrected  
 575 hindered settling). As expected it takes more time to build the cumulate layer to the same  
 576 maximum solid fraction starting from a lower solid fraction, and unsurprisingly with time the  
 577 starting solid fraction does not impact the maximum solid fraction reached in the simulation.  
 578 The major control over the maximum solid fraction in the cumulate layer is whether one  
 579 accounts for a finite compaction viscosity or not.

#### 580 4. Discussion: implications of the new settling model

581 The main purpose of this study has been to introduce the effect of compaction/consolidation  
582 viscosity in sedimentation. Hindered settling velocity describes the settling velocity accounting  
583 for interaction between particles with a *spatially uniform* particle density. Viscous dissipation  
584 due to particle settling is reflected in the reduced settling velocity relative to an isolated  
585 particle. In a continuum description, a spatial and/or temporal variation of the particle volume  
586 fraction in an REV introduces viscous dissipation in addition to that due to particle settling  
587 alone. We illustrate this with several simple or idealized examples. We show that this additional  
588 viscous dissipation rate can be expressed by a product of compaction or consolidation viscosity  
589 with the material derivative of the particle volume fraction describing the additional local  
590 average force acting on particles. We also provide some simple models to estimate the  
591 magnitude of the compaction viscosity, which is particularly large as the solid fraction increases  
592 toward the jamming condition.

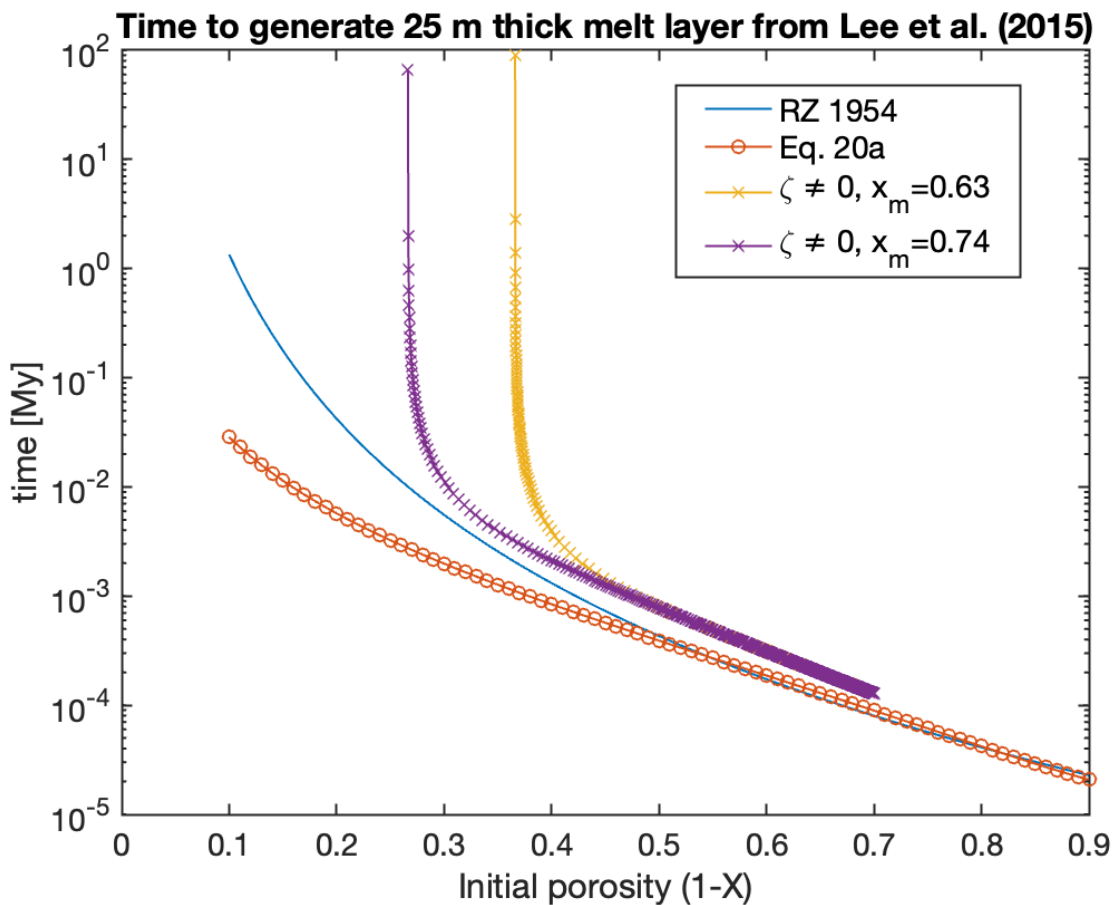
593 We see important consequences for the sedimentation front structure behavior. Variation of the  
594 hindered settling velocity with solid fraction has an important influence on the evolution of a  
595 settling front. An initially smooth front widens or narrows with time depending on whether the  
596 particle flux increases or decreases in the settling direction (e.g. Guazzelli and Morris, 2012;  
597 Kynch 1952). A narrowing front described solely by the variation of the hindered settling  
598 velocity with particle volume fraction steepens to form a nonphysical discontinuity.

599 With compaction viscosity present, we find that the front propagates at a slower speed than a  
600 discontinuous kinematic front. Dissipation associated with compaction viscosity limits how  
601 sharp the front can become, that is how rapidly the REV can gain or lose solid particles. Our  
602 results show a train of harmonic-like waves develops behind the front with an amplitude that  
603 decays with distance behind the front. The wavelength of the wave train and the distance over  
604 which it decays scales directly with the compaction length behind the front.

605 The combined effects of the variation of hindered settling velocity with solid volume fraction  
606 and the presence of a compaction viscosity lead to the prediction of complex behavior in the  
607 structure of a sedimentation front. An initial front can breakdown into a complex structure that  
608 allows the formation of layers with very low solid fraction.

609 Recently, Lee and Morton (2015) argued that hindered settling plays a key role in the separation  
610 of high silica melts from their crystal cargoes necessary to the formation of high silica granites  
611 (HSG). The arguments that favor hindered settling are (1) the range of estimated residual melt  
612 fraction in the left-over cumulates overlaps with values inferred for maximum packing and (2)  
613 the timescales of separation by hindered settling, unlike those of more melt-depleted  
614 compaction processes, are shorter or comparable to the cooling timescales of the host magma  
615 body. In a parallel study, Lee et al., compute these settling timescales from hindered settling  
616 laws based on the empirical correlation of Richardson and Zaki (1954). As a comparison, we  
617 recomputed their analysis using the same framework to calculate the time it takes to clear a

618 suspension of a given solid fraction  $X$  (or alternatively porosity  $1-X$ ) over a thickness of 25  
 619 meters (see Figure 9). The solid line is identical to that calculated in Lee et al. (2015), the line  
 620 with circle symbols is computed from the hindered settling function we use in this paper (Eq.  
 621 20a) and finally, the two trends with cross symbols shows actual solutions of our corrected  
 622 hindered settling model used to generate Figures 8C which accounts for the dissipation of  
 623 energy caused by changes in solid fraction, the yellow trend for the random maximum packing  
 624 for monodisperse spheres ( $\phi=0.37$ ) and the purple trend for the maximum close packing of  
 625 spheres ( $\phi=0.26$ ). Unlike the other two curves, the corrected model diverges at the maximum  
 626 packing fraction. It also shows that hindered settling times are generally longer, especially as the  
 627 solid fraction increase, than what is generally inferred from other models. Importantly, unlike  
 628 other models, it predicts that hindered settling cannot reduce porosity beyond the maximum  
 629 packing and that other, likely less efficient, processes are required to further compact a  
 630 cumulate. This again is consistent with the lowest trapped melt fraction estimated from  
 631 geochemistry being estimated around what is expected from maximum packing (Lee and  
 632 Morton, 2015).



633  
 634 Figure 9. Estimated time to clear a suspension with a given initial porosity over a layer of 25 meters of  
 635 thickness assuming a melt viscosity of  $10^5$  Pa s. The continuous (blue) line shows the time estimated  
 636 with the Richardson and Zaki (1954) hindered settling model, the line with the circle symbols (red)

637 shows the equivalent but for the different hindered velocity used here (Eq. 20a), the line with cross  
638 symbols (yellow) shows results from a numerical simulation (outputs from Figure 7c) with our  
639 compaction correction to hindered settling and a maximum packing  $X_m = 0.63$  and the purple line  
640 shows the same for the maximum close packing of spheres ( $X_m = 0.74$ ).

641

## 642 **Conclusions**

643 Particle settling is central to many fundamental processes in Earth and Planetary sciences. While  
644 the collective effect of particles on each other is known to affect the settling rate and has been  
645 parameterized as a hindrance function for many decades, we argue that the assumption that  
646 the settling rate is only function of the relative proportion of solids and fluid may fail to capture  
647 important dynamical behavior, particularly at high solid fractions. More specifically the  
648 existence and the growth of heterogeneities in particles spatial distribution (solid fraction)  
649 introduce an additional and traditionally overlooked contribution to energy dissipation through  
650 a stress term that introduces a consolidation or compaction viscosity.

651 This new consolidation or compaction term in the force balance causes remarkable dynamical  
652 features not seen with traditional hindered settling models. These features include the  
653 development of solid fraction waves at sharp fronts, with a structure that is controlled by a local  
654 balance between drag and compaction terms, in contrast with generic particle settling models  
655 where the force balance is restricted to drag and buoyancy. The balance between drag and  
656 compaction stresses introduces a characteristic length scale, the compaction length, into  
657 particle settling problems which affects the wavelength of the instability as well as the decay  
658 rate of the trailing waves behind the front.

659 We find that the resistance to compaction during particle settling (compaction viscosity)  
660 decreases significantly with decreasing solid fraction away from the maximum packing of  
661 particles, and that the strong dependence of the compaction viscosity on solid fraction allows  
662 generated waves to develop particle-depleted layers that grow over time. Thus, we expect that  
663 the compaction term introduced in particle settling not only generate dynamical waves at sharp  
664 fronts, but that these waves can cause bulk buoyancy and viscosity stratifications that may  
665 potentially initiate density overturns (Rayleigh-Taylor instability) if the growth rate of the latter  
666 exceeds the growth rate of the particle-depleted layer. This could affect convective heat and  
667 chemical transport at the top of magma bodies, where much of the heat driving crystallization  
668 occurs.

669 Another important feature associated with compaction term in the force balance relates to the  
670 growth and structure of particle cumulate layers at the base of closed systems, for example at  
671 the bottom of crystallizing magma bodies. The divergence of the compaction viscosity for  
672 settling at the maximum packing of the suspension caps the solid fraction at the maximum  
673 packing in the cumulate layer and slows the rate of settling (growth rate) of the cumulate layer  
674 compared to generic settling models. This behavior seem supported by geochemical and

675 textural analyses of cumulate layers feeding high silica granites, where the minimum trapped  
676 melt has been shown to coincide with the maximum packing of cumulate crystal phases.

677

## 678 **References**

679 Bachmann, O., and Bergantz, G.W. (2004), On the origin of crystal-poor rhyolites: extracted from  
680 batholithic crystal mushes, *Journal of Petrology*, vol. 45, p. 1565-1582.

681 Bachmann, O., and Huber, C., (2016), Silicic magma reservoirs in the Earth's crust, *American*  
682 *Mineralogist*, vol. 101, p. 2377-2404.

683 Batchelor, G.K., *An introduction to Fluid Dynamics*, Cambridge University Press, 1970.

684 Bergantz, G.W., and Ni, J., (1999) A numerical study of sedimentation by dripping instabilities in  
685 viscous fluids, *International Journal of Multiphase Flow*, Vol. 25, p. 307-320.

686 Boukaré, C.-E., E.M. Parmentier, and S.W. Parman (2018) Timing of mantle overturn during  
687 magma ocean solidification, *Earth Planet Sci Lett* 491, 216-225

688 <https://doi.org/10.1016/j.epsl.2018.03.037>.

689 Bercovici, D., Y. Ricard, and G. Schubert (2001) A two phase model for damage and compaction,  
690 *J. Geophys. Res.* 106, 8887-8906.

691 Costa, A., L. Caricchi, and N. Bagdassarov (2009) A model for the rheology of particle-bearing  
692 suspensions and partially molten rocks, *Geochem. Geophys. Geosys.* 10

693 doi:10.1029/2008GC002138.

694 Culha C, Suckale, J., Keller, T., and Qin, Z., (2020) Crystal fractionation by crystal-driven  
695 convection, *Geophysical Research Letters*, vol. 47, e2019GLO86784.

696 Dasgupta, T., Mukherjee, S., (2020) Porosity in Carbonates. In: *Sediment Compaction and*  
697 *Applications in Petroleum Geoscience. Advances in Oil and Gas Exploration & Production.*  
698 Springer.

699 Davis, R.H., and Acrivos, A. , (1985), Sedimentation of noncolloidal particles at low Reynolds  
700 numbers, *Ann. Rev. Fluid. Mech.*, vol. 17, p. 91-118.

701 Drew, D.A. (1983) Mathematical Modelling of Two Phase Flow, *Ann. Rev. Fluid Mech.* 15, 261-  
702 291.

703 Elkins-Tanton, L. T. (2012) Magma Oceans in the Inner Solar System, *Ann. Rev Earth and Planet.*  
704 *Sci.* 40:113-139, <https://doi.org/10.1146/annurev-earth-042711-105503>.

705 Fitch, B. (1983) Kynch theory and compression zones, *AIChE J.* 29, 940.

706 Faroughi, S.A., and Huber, C., Unifying the relative hindered velocity in suspensions and  
707 emulsions of non-deformable particles, *Geophysical Research Letters*, vol. 42, 2015, p. 53-59.

708 Faroughi, S.A., and Huber, C., Rheological state variables: a framework for viscosity  
709 parameterization in crystal-rich magmas, *Journal of Volcanology and Geothermal Research*, vol.  
710 440, 2023, p. 107856.

711 Guazzelli, E., and Morris, J.F., *A Physical Introduction to Suspension Dynamics*, Cambridge  
712 University Press, 2012.

713 Hess P.C. and E.M. Parmentier (1995) A model for the thermal and chemical evolution of the  
714 Moon's interior: Implications for the onset of mare volcanism, *Earth Planet Sci Lett* 134, 501-  
715 514. [https://doi.org/10.1016/0012-821X\(95\)00138-3](https://doi.org/10.1016/0012-821X(95)00138-3)

716 Lee and Morton

717 Hildreth, W., and Wilson, C.J.N. (2007), Compositional zoning of the Bishop Tuff, *Journal of*  
718 *Petrology*, vol. 48, p. 951-999.

719 Huguet, L., M. Le Bars, R. Deguen (2023) A laboratory model for iron snow in planetary cores,  
720 *Geophys. Res. Lett.* 50, doi.org/10.1029/2023GL105697.

721 Kynch, G. J. (1952) "A theory of sedimentation," *Trans. Faraday Soc.* 48, 166.

722 Lee, C.T.A. and D.M. Morton (2015) High silica granites: Terminal porosity and crystal settling in  
723 shallow magma chambers, *Earth Planet. Sci. Lett.* 409, 23-31,  
724 <https://doi.org/10.1016/j.epsl.2014.10.040>

725 Lister, J.R. and R.C. Kerr (1989) The effect of geometry on the gravitational instability of a  
726 buoyant region of viscous fluid, *J. Fluid Mech.* 202, 577-594.

727 Lowman, N.K., and M.A. Hoeffler (2013) Dispersive shockwaves in a viscously deforming media,  
728 *J. Fluid Mech.* 718, 524-557.

729 Marsh, B. and M. Maxey, On the distribution and separation of crystals in convecting magma,  
730 *Journal of Volcanology and Geothermal Research*, 1985, V. 24, p. 95-150.

731 Martin, D., and Nokes, R., (1989) A fluid-dynamical study of crystal settling in convecting  
732 magmas, *Journal of Petrology*, Vol. 30, p. 1471-1500.

733 McKenzie, D. (1984) The generation and compaction of partially molten rock, *J. Petrology* 25,  
734 713-765.

735 Moore, C.H., (1989) Carbonate diagenesis and porosity. In: *Developments in Sedimentology* 46,  
736 Elsevier.

737 Richardson J.F. and W.N. Zaki (1954) The sedimentation of a suspension of uniform spheres  
738 under conditions of viscous flow, *Chemical Engineering Science*, Vol. 3, p. 65-73.

739 Rubie, D. C., H. J. Melosh, J. E. Reid, C. Liebske, and K. Righter (2003), Mechanisms of metal-  
740 silicate equilibration in the terrestrial magma ocean, *Earth Planet. Sci. Lett.*, 205, 239–255.  
741  
742 Shearer, C.K., et al., (2006) Thermal and magmatic evolution of the Moon, *Reviews in*  
743 *Mineralogy and Geochemistry*, 365-518.

744 Stevenson, D.J. (1990) Fluid dynamics of core formation, in: H. Newsom, J.H. Jones (Eds.), *The*  
745 *Origin of the Earth*, Oxford Press, London, pp. 231–249.

746 Solomatov, V.S. (2000) Fluid dynamics of magma oceans, *Origin of the Earth and Moon* (R.  
747 Canup, K. Righter, eds) Univ. of Arizona Press, Tucson 323-338.

748 Spiegelman, M., (1993) Flow in deformable porous media. *J. Fluid Mech.* 247, 39-63.

749 Stokes, G.G., On the effect of the internal friction of fluids on the motion of pendulums,  
750 *Transactions of the Cambridge Philosophical Society*, vol. IX, 1851, p[8]

751 Wallis, G.B., *Two-phase flow*, Dover Publications, 2020.

752 Whitehead, J.A. (1988) Fluid Models of Geological Hotspots, *Ann. Rev. Fluid Mech.* 20:61-87.

753 Wilcox and Whitehead (1991) Rayleigh-Taylor instability of an embedded low viscosity fluid  
754 layer, *J. Geophys. Res.* 96, 12193.

755 Zick, A.A., and Homsy, G.M., Stokes flow through a periodic array of spheres, *Journal of Fluid*  
756 *Mechanics*, vol. 115, 1982, p 13-26.

757

758

759

## 760 **Appendix 1: Numerical methods**

761 The mass and momentum conservation equations in one spatial dimension, (12) and (13), are  
762 solved using a finite standard volume formulation. Centered differences and linear  
763 interpolations are employed as required. Conservation of solid volume fraction (12) is solved  
764 using forward differences in time and conserving upwind approximations for advection.  
765 Numerical diffusion introduced by upwind approximations is minimized by using finely spaced  
766 grids in the simple one-dimensional problem. Most examples presented above were computed  
767 with 4096 grid points. Refinement to 8192 grid points showed at most a fraction of 1% change  
768 in computed values. An advantage of the upwind approximation is its simplicity and the stability  
769 of forward time stepping. The time step used was significantly less than the CFL time step to  
770 suppress numerical instability arising from time variable coefficients in the momentum  
771 equation.

## 772 **Appendix 2: Nondimensionalization**

773 The equations solved were expressed in nondimensional form based on an appropriate length  
 774 scale  $L$  and single particle settling velocity  $V_{stokes}$ . Time in the solid phase conservation  
 775 equation is accordingly nondimensionalized  $L/V_{stokes}$ . The hindered settling velocity  $V_H(X) =$   
 776  $V_{stokes}H(X)$  is derived from the hindrance function  $H(X)$  and  $V_{stokes}$  which is proportional to  
 777 the square of the particle size and inversely with the fluid viscosity  $\mu_f$ . For spherical particles is

$$778 \quad V_{stokes} = \frac{2 \Delta \rho g a^2}{9 \mu_f}$$

779 The nondimensional momentum equation becomes

$$780 \quad \frac{X}{(1-X)H(X)} V_s + X - \frac{V_{stokes} \mu_f}{\Delta \rho g L^2} \frac{\partial}{\partial z} \left[ X \frac{\zeta}{\mu_f} \frac{\partial V_s}{\partial z} \right] = 0$$

781 where  $L$  may be an appropriate geometric length.

782 In the absence of such a length we choose

$$783 \quad L \equiv \delta_{ref} = \sqrt{\frac{V_{stokes} \mu_f}{\Delta \rho g}} = \frac{\sqrt{2}}{9} a$$

784 where  $\delta_{ref}$  is a reference value of the compaction length removes all explicit nondimensional  
 785 parameters from both the momentum and solid fraction conservation equations.

786